Wearable Core Body Temperature Sensor and Its Application

Yujiro Tanaka

1 Introduction

The core body temperature (CBT) is the temperature deep inside the body (e.g., the rectum, brain, heart, and liver). The CBT is essential for our daily health management. The CBT changes depending on the health condition, age, individual, body's internal clock, and behavior. The heatstroke or catching a cold can lead to a high temperature, while a low temperature can lead to hypothermia. In terms of the CBT's time dependence, it has a 24-h rhythm that is strongly related to the body's internal clock [1]. The CBT reaches its minimum (nadir) in the night or few times before waking up and its maximum is between 2 and 7 pm, as shown schematically in Fig. 1. The time of the nadir is used as a parameter for evaluating the body's internal clock, which is strongly related to the blood melatonin level [2]. Disorders of the internal clock, which are related to problems such as diabetes, cancer, and sleep disorders, induce metabolic aberrations and depression. Such disorders also decrease exercise and work performance [1–9]. Therefore, continuous CBT measurement could be a valuable tool for managing the daily physical condition and detecting diseases in their early stages.

2 Core Body Temperature

The temperature in the pulmonary artery is the gold standard for the core temperature, but the rectal temperature (described below) is used in clinical practices. In recent years, the esophageal, tympanic, and rectal temperatures have been used as the main

Y. Tanaka (✉)
NTT Basic Research Laboratories, 3-1, Morinosato Wkamiya, Atsugi-Shi, Kanagawa 243-0198, Japan
e-mail: yujiro.tanaka@ntt.com

K. Mitsubayashi (ed.), *Wearable Biosensing in Medicine and Healthcare*,
https://doi.org/10.1007/978-981-99-8122-9_11

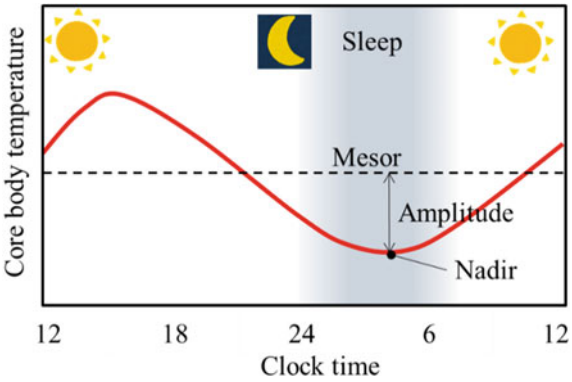

Fig. 1 CBT behavior over the day

CBT indicators. In addition, the sublingual mouth and axilla have been used as CBT measurement sites. Below, we summarize the characteristics of each site [10–13].

2.1 Rectal Temperature

As stated before, the temperature of the rectum is used as a gold standard in clinical practices and research on the CBT and circadian rhythm. The rectal temperature is measured by inserting a sensor probe a few centimeters into the rectum. It indicates the temperature of internal organs located deep in the body, with a heat source derived from the iliac artery and iliac vein. The rectal temperature is higher than the temperatures of other sites because of the rectum's isolation from ambient conditions and low heat dissipation. It also changes more slowly than the other temperatures. Although it provides an accurate CBT, the measurement is stressful and potentially risky because of rectal damage and infection; moreover, it is affected by the presence of stool, inflammation around the rectum, and heat-producing activities by microorganisms.

2.2 Oral Temperature

The oral temperature is measured at the posterior sublingual pockets. The heat source is a branch of the external carotid artery. This temperature can be affected by the sensor position, vascular activity in the sublingual area, salivation, food and fluid intake, and breathing. Stabilization of the temperature requires a few minutes.

2.3 Axillary Temperature

The axillary temperature is relatively lower than the temperatures at the other sites. While it can be measured easily, it is strongly affected by the ambient conditions, blood flow, sweat, and sensor position. Also, temperature differences of up to 1.4 °C have been reported between the right and left axillas. Moreover, the axillary temperature takes approximately 5 min to stabilize.

2.4 Tympanic Temperature

The tympanic temperature is the temperature of the eardrum, whose heat source is the blood supply from the internal and external carotid arteries. Compared with the other sites, it has less of a relationship to metabolic activity. An indirect monitoring technique was developed by using infrared radiation from the eardrum. Because of its usability and accuracy, it has been used for monitoring CBT changes during physical exercise. However, the ambient temperature and convection affect the tympanic temperature.

3 Noninvasive Core Body Temperature Monitoring Technique

3.1 Noninvasive Techniques

As mentioned above, the rectal temperature is reliable and stable against ambient conditions. However, a natural body cavity such as the rectum is not suitable for direct, long-term measurement of the core body temperature (CBT) by insertion of a sensor probe. Such placement of a sensor probe is stressful for a person, especially while awake, and it has the accompanying risks of infection and damage to the rectal cavity. To address this issue, alternative noninvasive techniques have been explored, including in-ear, ingestible, and skin-attachable sensors [14–26]. In-ear sensors cause discomfort, and the measurements are sometimes influenced by environmental conditions and movements. Ingestible sensors indicate the CBT similarly to the rectal temperature; however, they are limited by the duration of monitoring and the difficulty of collecting the sensor after use. On the other hand, skin-attachable sensors, which indirectly estimate the CBT by using the skin temperature and heat flux, avoid these disadvantages.

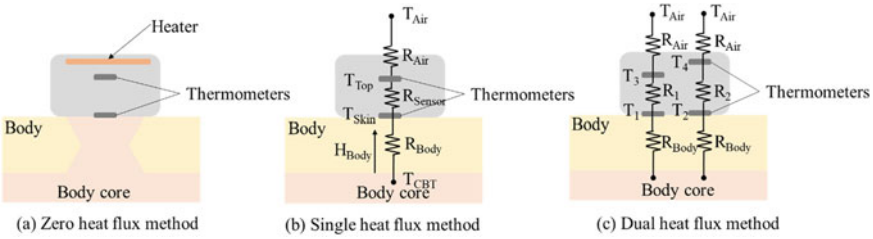

Fig. 2 Comparison of skin-attachable CBT sensors

3.2 Skin-Attachable Sensing Techniques

The temperature of the skin does not satisfy the state of thermal equilibrium with the body core. Therefore, it forms a partial temperature gradient from body core to skin [14]. Therefore, it is necessary to devise a way to compensate for this temperature gradient.

3.2.1 Zero-Heat-Flux Method

A representative technique for noninvasive CBT measurement, called the zero-heat-flux method, was proposed by Togawa et al. [18] and by Fox et al. [19]. This technique makes use of a heater to heat the skin and compensates the dissipation of heat with respect to the ambient conditions, as shown in Fig. 2a. It provides an isothermal region from the skin to the body core, which makes the skin temperature close to the CBT. This technique is used for monitoring the CBT during surgery and in intensive care units [20–22]. Sensors based on this technology have been commercialized by TERUMO Co. (CoreTemp), and 3 M (Bair Hugger). However, it requires a heater, which consumes considerable electrical power and usually requires an AC power supply. Thus, it is difficult to monitor the CBT all day long. Moreover, it has been pointed out that this technique might measure the temperature of the hottest part of the measurement site.

3.2.2 Heat-Flux Method

The technique with sensors containing two or four thermometers was proposed [23–26]. The heat-flux method uses the skin temperature and the heat flux obtained from a sensor attached to the skin, as shown in Fig. 2b, c. The CBT is obtained from the following equation based on the body's unknown thermal resistance:

$$T_{CBT} = T_{\text{Skin}} + R_{\text{Body}} H_{\text{Body}}, \tag{1}$$

where R_{Body} is a constant coefficient related to the thermal properties of the body and the sensor, T_{Skin} is a temperature measured at the skin surface, and the H_{Body} is the heat flux measured at the skin surface. The heat flux H_{Body} is sometimes assumed to be proportional to the temperature difference between two points T_{Skin} and T_{Top}. On the other hand, it is necessary to calibrate R_{Body} at the beginning of monitoring by using a reference temperature (e.g., the tympanic temperature) in the single heat flux method (Fig. 2b). To obtain the R_{Body}, a sensor with four thermometers solves this issue by using two different thermal resistances, as shown in Fig. 2c, which is called the dual-heat-flux method. As reported by Kitamura et al., the CBT is estimated by assuming a 1-dimensional thermal equivalent circuit with two thermally isolated heat paths [23], as shown in (Fig. 2c). From the skin temperatures and heat fluxes along the two heat paths, Eq. (1) can be obtained for each path. Then, the body's unknown thermal resistance can be obtained by combining the two equations via the following equation:

$$T_{CBT} = T_1 + \frac{(T_1 - T_2)(T_1 - T_3)}{K(T_2 - T_4) - (T_1 - T_3)}, K = \frac{R_1}{R_2}. \tag{2}$$

This technique provides fully passive CBT measurements and is suitable for daily continuous measurement, although it assumes that the sensors are used in a stable environment or a hospital. Also, the heat is assumed to flow vertically from the point of skin contact, although lateral heat flow is also commonly caused by traveling, air conditioning, and other factors.

3.3 Problems of Skin-Attachable Sensor

According to Pennes' models of heat transfer in humans [27], the CBT estimation procedure is expressed as follows:

$$\frac{\partial T}{\partial t} = \frac{k_{\text{tissue}}}{C_{\text{tissue}}\rho_{\text{tissue}}}\Delta T + \rho_{\text{Blood}}C_{\text{Blood}}w\left(T_{\text{Array}} - T\right) + Q, \tag{3}$$

where T, t, k, ρ, C, w, and Q denote the temperature, time, thermal conductivity, density, specific heat, circulation, and internal heating, respectively, and Δ is the Laplace operator. The left term on the right side of Eq. (3) can be ignored if the body temperature changes slowly. Moreover, by choosing a site where the circulation and internal heating are small, the second and third terms on the right can also be ignored. Finally, by assuming that the tissue has uniform thermal properties and the heat travels vertically, the following simplified heat transfer equation can be obtained:

$$\frac{d^2T}{dz^2} = 0, \tag{4}$$

where z is the depth coordinate. This result indicates that the temperature distribution is linear from the body core to the skin. Thus, the CBT can be obtained from the skin temperature and the heat flux at the skin, as mentioned above. However, while the heat-flux method enables fully passive CBT estimation without any external heater, it is difficult to satisfy the above assumptions for a person being monitored in daily life. Ambient convection induces a lateral heat flow, which immediately increases the estimation error. Moreover, the sensor's presence also causes heat to travel laterally.

3.4 Design of Skin-Attachable Sensor [33]

To leverage the advantages of the heat-flux method while addressing the issue of lateral heat flow, we designed a novel structure for a CBT sensor. Ambient convection causes the heat flux to be overestimated or underestimated as shown in Eq. (5) and Fig. 3. Such convection results in heat dissipation, where heat is lost passively because of ambient air flow due to external sources such as air conditioning and activities such as walking or running. For continuous CBT monitoring in daily life, it is thus necessary to reduce the heat loss. Hence, we first focus on the problem of mitigating lateral heat transfer by designing the sensor's structure accordingly. Specifically, the design was developed through topology optimization, which provides a systematic design procedure and has become widely used in various fields (e.g., thermo-fluid dynamics) [28–31].

$$T_{CBT} = T_{\mathrm{Skin}} + R_{\mathrm{Body}}\left(H_{\mathrm{Body}} - H_{\mathrm{Loss}}\right), \tag{5}$$

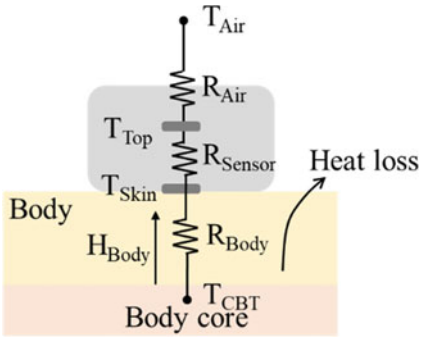

Fig. 3 Schematic images of the heat loss

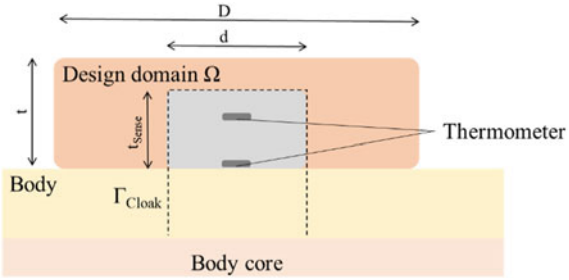

Fig. 4 Schematic cross section of the CBT sensor

3.4.1 Numerical Computation

Model

Figure 4 shows a schematic cross section of a model for numerical computation of the CBT sensor. The sensor has a cylindrical chassis with diameter D = 30 mm and height t = 5 mm, which were determined as optimal values for mobility and usability. The chassis contains a heat-resistant substrate which has two thermometers. In the figure, the aluminum structure is allocated in the design domain Ω for reducing the heat loss. The boundary conditions of the following model were considered for estimating the heat transfer coefficient H at the boundary. The CBT sensor was assumed to be exposed to air flow due to air conditioning, walking, or running. Specifically, the wind speed V_{In} was assumed to be 5 m/s (corresponding to a running speed of 18 km/h). The distance from the skin to the body core, t_{Body}, was assumed to be 10 mm. To simplify the optimization for the fluid and heat transfer interaction system, we used the heat transfer coefficient H at the boundary with the ambient air to incorporate convectional heat transfer. The relationship between the wind speed and H was estimated from the Nusselt number Nu by its definition, Prandtl number Pr, and Reynolds number Re, as follows:

$$\mathrm{Pr} = \frac{Cp_{\mathrm{Air}}\mu_{\mathrm{Air}}}{\lambda_{\mathrm{Air}}}, \tag{6}$$

$$\mathrm{Re} = \frac{\rho_{\mathrm{Air}} V_{\mathrm{In}} t_{\mathrm{Body}}}{\mu_{\mathrm{Air}}}, \tag{7}$$

where V_{In}, L, ρ_{Air}, μ_{Air}, and λ_{Air} denote the wind speed, characteristic length, air density, air viscosity, and thermal conductivity, respectively. For laminar flow, the Nusselt number Nu is given by [32]

$$\mathrm{Nu} = 0.664 Re^{1/2} Pr^{1/3}. \tag{8}$$

Finally, by combining Eqs. (6), (7), and (8), we obtain the heat transfer coefficient as a function of the wind speed V_{In}:

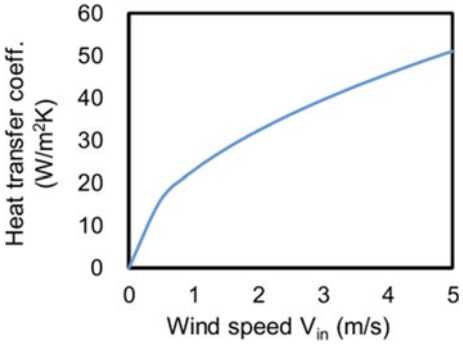

Fig. 5 Relationship between the heat transfer coefficient and wind speed

$$\mathrm{H} = 0.664 Pr^{1/3} \sqrt{\frac{\rho_{\mathrm{Air}}}{\mu_{\mathrm{Air}}}} \sqrt{\frac{V_{\mathrm{in}}}{L}}. \tag{9}$$

Figure 5 shows the relationship between the heat transfer coefficient and the wind speed, with the diameter of the CBT sensor used as the characteristic length L. As seen in the figure, the heat transfer coefficient ranges from 0 to 50 W/m^{2}K when V_{In} ranges from 0 to 5 m/s.

Problem Setting for the Topology Optimization

The structure's design is explained in this section. To reduce the heat loss, an aluminum structure was designed by using topology optimization to reduce the estimation error. In this optimization, the objective was to minimize the heat flux at the boundary:

$$J = \int_{\Gamma_{\mathrm{Cloak}}} H d\Gamma. \tag{10}$$

This objective aims to directly reduce the heat loss. The sensitivity of the objective to changes in the design variables was required for the optimization and was obtained by adjoint sensitivity analysis. The optimization procedure was the method of moving asymptotes (MMA). The numerical computation was performed using COMSOL Multiphysics 5.5.

The steady-state heat conduction equation is used as follows.

$$\nabla\left(k_\gamma \nabla T\right) = 0. \tag{11}$$

where k is the thermal conductivity (with a subscript indicating the material, e.g., Al for aluminum), γ is the design variable, and q is a parameter for the nonlinearity of interpolation, such that the nonlinearity increases as q decreases. The material's thermal conductivity distribution was optimized via a spatially defined density design

Table 1 Parameters in the computation

Variable	Variable	Value
Sensor height	t	5 mm
Sensor diameter	D	30 mm
Substrate height	t_{Sub}	4 mm
Substrate diameter	d	8 mm
Body depth	t_{Body}	10 mm
Ambient temp	T_{in}	20 °C
CBT	T_{Body}	37 °C
Wind speed	V_{In}	5 m/s
Calculation diameter	L	80 mm

Table 2 Thermo and fluid physical parameters

Part	Thermal conductivity k (W/mK)
Air	0.02
Body	0.37
Aluminum	204

variable γ, which ranged from 0 to 1. The thermal conductivity k_γ was interpolated as follows:

$$k_\gamma = k_{Al} + (k_{\text{Air}} - k_{Al})\gamma \frac{1+q}{\gamma+q}, \tag{12}$$

Table 1 lists the parameters used in the optimization. Table 2 lists the thermophysical parameters used in the numerical computation. A typical problem that arises in topology optimization is a gray scale for the material distribution, which means a porous structure and a lower fabrication tolerance. To avoid this issue, a Helmholtz PDE filter,

$$\gamma_f = \gamma + R_{\text{min}}^2 \Delta\gamma_f, \tag{13}$$

and a smoothed Heaviside projection are used [28],

$$\gamma = \frac{\tanh\left(\beta\left(\gamma_f - \theta_\beta\right)\right) + \tanh\left(\beta\theta_\beta\right)}{\tanh\left(\beta\left(1-\theta_\beta\right)\right) + \tanh\left(\beta\theta_\beta\right)}, \tag{14}$$

where β is a parameter determining the projection's steepness, and θ_β is a threshold parameter, which was fixed at 0.5. In this work, we set β as 15, and the initial design variable γ was 0.5.

3.4.2 Optimized Structure and Accuracy of Topology Optimization

The initial structure and the resulting optimized aluminum structure are shown in Fig. 6a, b. The red region represents the optimized structure, which resembles a truncated cone with a hole at the top. Unfortunately, the structure's complex curves and inconsistent thickness made fabrication difficult and decreased the accuracy of numerical computation. To improve the accuracy and fabrication tolerance, we simplified the structure to have a uniform thickness of 0.5 mm and a smooth surface. The diameter of the hole in the truncated cone was 2 mm. Figure 6c shows the estimation errors for various diameters of the cone's base and hole. The estimation error gradually decreased with a smaller base diameter D or hole diameter d, and it bottomed out at approximately 2 mm. For evaluation, as shown in Fig. 7, the (a) heat loss and (b) estimation error were calculated numerically as a function of the wind speed V_{In}. The maximum wind speed was $V_{\mathrm{In}} = 5$ m/s. The coefficient for estimating the CBT, R_{Sensor}, was obtained from T_{skin} and H_{Body} at $V_{\mathrm{In}} = 1$ m/s. The blue and orange points respectively indicate the results with and without the optimized aluminum structure. In either case, the heat loss H_{Loss} and the estimation error increased with the wind speed, but they were effectively reduced when the optimized structure was used. The maximum estimation errors with and without the structure were 0.1 and 0.4 °C, respectively, at $V_{\mathrm{In}} = 5$ m/s.

3.5 *In-Vitro Experimental Verification [34]*

The proposed structure's effectiveness was preliminarily verified through an in-vitro experiment using a phantom to simulate the body's thermal conductivity.

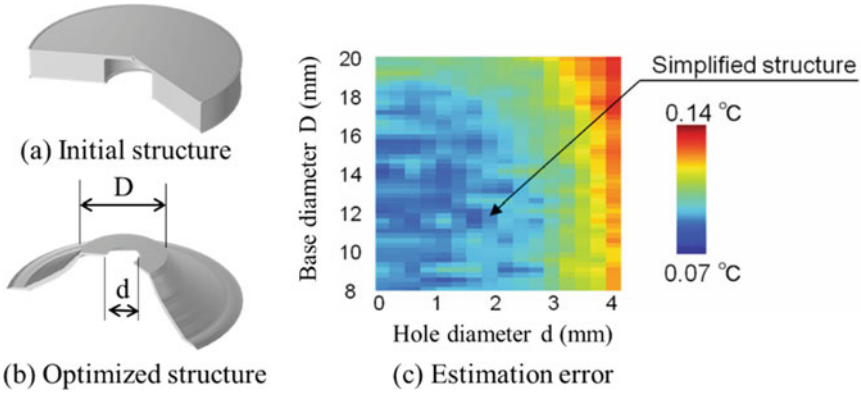

Fig. 6 Optimized aluminum structure. **a** and **b** are the initial structure and the resulting optimized aluminum structure. **c** Estimation errors for various values of the hole diameter d and the base diameter D

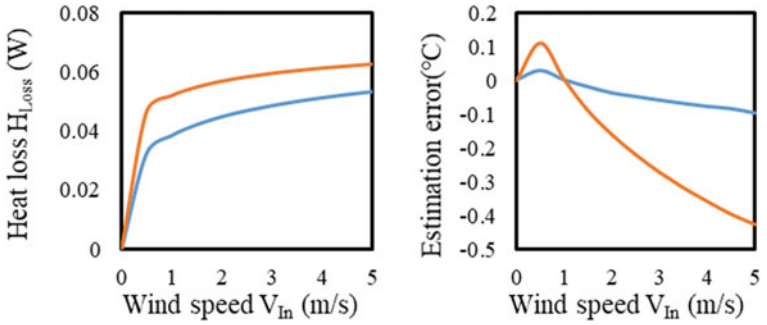

Fig. 7 Comparison of the **a** heat loss and **b** estimation error with (blue) and without (orange) the optimized aluminum structure, as a function of the wind speed V_{In}

3.5.1 Experimental Setup

The proposed CBT sensor with the aluminum structure to reduce the heat loss was fabricated as shown in Fig. 8. The sensor chassis' diameter and height were 31 and 5.1 mm, respectively. Its top and bottom were made of 0.1-mm-thick polyethylene terephthalate (PET), and its sides were made of 0.5-mm-thick polylactic acid (PLA). The thickness of the aluminum structure was 0.5 mm across the entire structure. The height of the heat resistance substrate was 5 mm, and the diameter of the hole in the truncated cone was 2 mm. The heat-resistant substrate was made of PLA and had two platinum resistance thermometers integrated into it. The gap d between the two thermometers was 2 mm, and each thermometer's diameter and length were 0.4 and 1 mm, respectively. The temperature of a hotplate, $T_{Hotplate}$, was measured every 1 s by a thermometer and read out from the thermometer by a data logger. The coefficient R_{Sensor} was estimated from the temperatures T_{skin} and T_{top} measured by the two thermometers. The heat flux H_{Body} was assumed proportional to the temperature gap T_{skin}-T_{top}:

$$H_{\mathrm{Body}} \propto T_{\mathrm{Skin}} - T_{\mathrm{top}}. \tag{15}$$

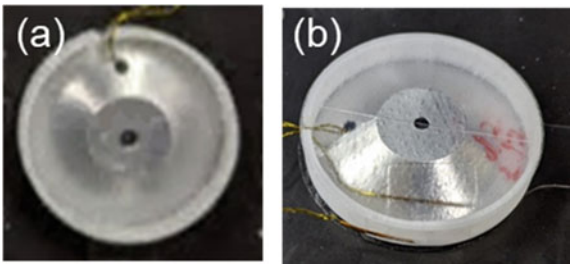

Fig. 8 Illustrations of the fabricated CBT sensor: **a** top view image, **b** bird's eye view image

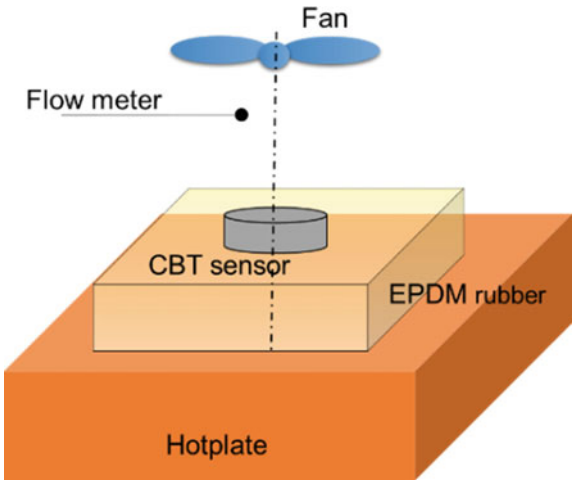

Fig. 9 In-vitro experimental configuration with a hotplate to simulate the CBT

By substituting Eq. (15) into Eq. (1), we obtained the coefficient R_{Sensor} from the hotplate temperature at a specific time:

$$R_{Sensor} = \frac{T_{Hotplate} - T_{Skin}}{T_{Skin} - T_{Top}}. \tag{16}$$

As for the phantom representing the body, shown in Fig. 9, we used EPDM rubber with a thickness of 10 mm because its thermal conductivity of 0.36 W/m/K is similar to that of the human body (0.37 W/m/K). The phantom was placed on the hotplate, and the CBT sensor was placed on the phantom. The ambient temperature was room temperature (20 °C). Convection was induced by a fan placed above the sensor, and the wind speed was measured with a hot-wire anemometer.

3.5.2 In-Vitro Experimental Results and Discussion

The hotplate temperature $T_{Hotplate}$ was varied from 32 to 42 °C, and the wind speed V_{In} was varied from 0 to 5 m/s. The coefficient R_{Sensor} was 2.45 in the experiment, whereas the computed value was 2.5. This discrepancy may have been due to the contact heat resistance between the sensor and phantom and the size of the thermometers. The relationship between the estimated and hotplate temperatures is shown in Fig. 10a, while the root-mean-square error (RMSE) with respect to the wind speed is shown in Fig. 10b. The amplitude of the CBT was about 1 °C [34], which shows that the proposed sensor can be used to monitor the CBT over the course of a day. In addition, Fig. 10c shows a Bland–Altman plot, which is a tool to assess whether measurements are contaminated with systematic errors. Specifically, it comprises a scatter plot of the difference between two measured values on the y-axis and the mean of the two values on the x-axis. The scatter plot enables visual evaluation of the presence and

degree of systematic errors. If there is no systematic error, i.e., only random error, the plot will show a distribution that varies both positively and negatively from the x-axis. If there is a fixed systematic error, the plot will show a distribution that is biased either positively or negatively from the x-axis, as seen in the figure here. Lastly, a proportional error will yield a fan-shaped distribution where the difference between the two measurements increases as the value on the x-axis increases. As seen in Fig. 10c, the systematic error increased with the hotplate temperature. To summarize these results, although systematic errors could arise depending on the hotplate temperature, the proposed structure successfully decreased the wind's effect.

Lastly, we discuss the heat loss reduction with the optimized aluminum structure comprising a truncated cone with a hole. Figure 11 shows a schematic image of the heat flow around the CBT sensor on temperature field. The heat flux H_{Body} comes from the body core, and estimation error is induced by the heat loss H_{Loss}. However, the aluminum structure collects heat H_{Plus} from the sensor's surrounding region. The collected heat is then isolated from the heat flux because the foot of the truncated cone is far enough from the heat-resistant substrate. Thus, the collected heat H_{Plus} increases the temperature of the region surrounding the substrate, and it mitigates the heat loss H_{Loss}. Additionally, the hole in the truncated cone enables the heat flux H_{Body} to be easily released into the ambient air.

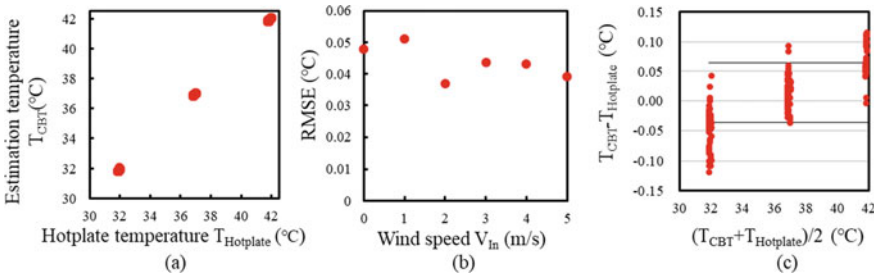

Fig. 10 In-vitro experimental evaluation of the CBT sensor: **a** response curve of the CBT sensor with respect to the hotplate temperature, **b** root-mean-square error (RMSE) versus wind speed, and **c** Bland–Altman plot

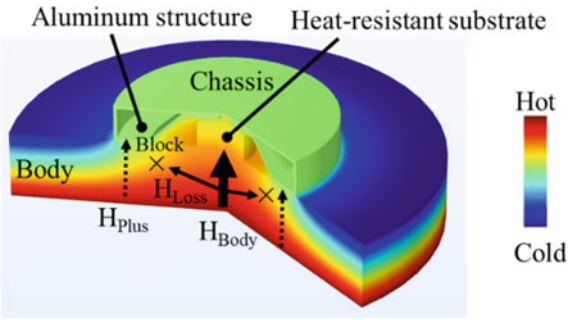

Fig. 11 Schematic image of the heat flow around the CBT sensor on temperature field

3.6 *In-Vivo Experimental Verification*

Through the in-vitro experiment described above, we demonstrated that a truncated cone structure made of a material with high thermal conductivity can reduce the lateral heat flow. Next, to address the assumptions of steady approximation and that circulation and internal heating can be ignored, we conducted an in-vivo experiment.

3.6.1 Examination of Measurement Site

It is pointed out that the method of estimating CBT from the skin surface might measure the temperature of the hottest part of the measurement site [35]. If there are many muscles at the position where the sensor is attached, the estimated temperature may be affected by heat production due to muscle activity. As the forehead does not have large muscles and is close to the cerebrum, where the thermoregulatory center exists, it is thought to reflect the brain temperature, thus making it a suitable sensor attachment site.

3.6.2 CBT Monitoring During Fanning

Figure 12 shows a photograph and a schematic of the skin-attachable sensor. In this in-vivo experiment, the sensor's diameter and thickness were 30 and 5 mm, respectively. The sensor again had a truncated cone structure made of aluminum with a thickness of 0.5 mm to reduce the lateral heat flow. Two thermometers were integrated into the cylindrical polymer, which had a diameter of 8 mm, and the vertical distance between the two thermometers was 2.5 mm. The temperature difference between the thermometers was taken to be H_{Body} in the CBT estimation, as it was assumed to be proportional to the heat flux. Six healthy volunteers participated in this study. The skin-attachable sensor was placed on the forehead with double-sided tape. The tympanic temperature was monitored by an infrared thermometer to provide a reference temperature, because it is easily measured and highly correlated with the CBT [36, 37]. Because the tympanic temperature is easily affected by the ambient environment [34, 38, 39], the volunteers wore earmuffs to prevent this effect. The study was performed at an ambient temperature of 28 °C and 50% humidity. After 1 h delay for stabilization of the skin-attachable sensor, each volunteer was exposed to wind (1 m/s) produced by an electric fan and performed light exercise on a bicycle ergometer. The wind exposure induced a lateral heat flow. At the start of the experiment, R_{Body} was calculated from the reference tympanic temperature.

Figure 13a shows typical results for the estimated CBT and tympanic temperature behavior. The relationship between the tympanic temperature and CBT estimated at the forehead is shown in Fig. 13b. The RMSE was 0.14 °C, and the correlation coefficient was 0.96. The sensor results showed good agreement with the tympanic temperature. A Bland–Altman plot is shown in Fig. 13c.

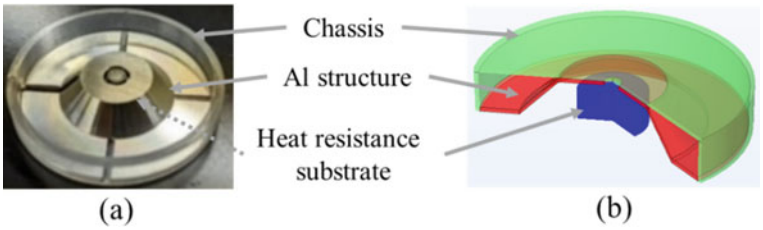

Fig. 12 **a** Photograph and **b** schematic of the skin-attachable sensor designed via topology optimization

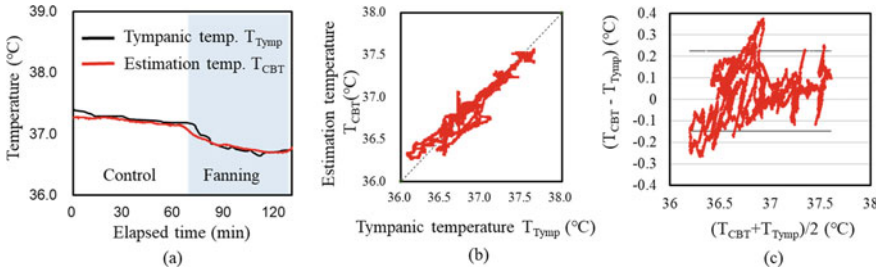

Fig. 13 In-vivo evaluation of the CBT sensor: **a** Typical CBT behavior during fanning, **b** response curve of the CBT sensor with respect to the tympanic temperature, and **c** Bland–Altman plot

3.7 Applications

In this section, we describe an application of system integration with the proposed skin-attachable CBT sensor and demonstrations of its use for monitoring sleep, jet lag induced by a long flight, and fever after COVID-19 vaccination.

3.7.1 System Integration

To monitor the CBT in daily life, we developed a sensor device that integrates a data storage memory, communication module, and battery. Table 3 lists the device specifications. As shown in Fig. 14, the circuit board and battery are stacked on the proposed sensor structure. The sensor has a diameter of 33 mm, a height of 8 mm, and a weight of 10 g. It can communicate with a computer or a smartphone, as seen in Fig. 14, via Bluetooth Low Energy (BLE). The coin-type battery (RC2032) enables continuous monitoring of the core body temperature for up to 60 days. In addition, the device is waterproof to allow its use in everyday life.

Table 3 CBT sensor device specifications

Size	33 mm Φ × 8 mm thickness
Weight	10 g (including battery)
Sampling rate	1–60 s
Communication	Bluetooth low energy
Power supply	Coin-type battery (CR2032)
Continuous measurement time	4–60 days

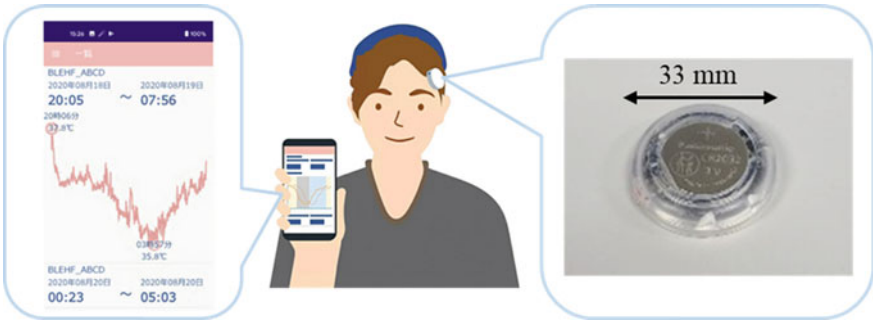

Fig. 14 Photograph of the CBT sensor device, and a screenshot of the smartphone application

3.7.2 Sleep Monitoring

As mentioned above, the CBT drops during sleep, and the time when it reaches its minimum is an index for evaluating the circadian rhythm. Accordingly, we attached a sensor to the forehead during sleep to measure changes in the CBT, along with a tympanic thermometer for comparison. In the results shown in Fig. 15a, the red line indicates the eardrum temperature, and the black line indicates the temperature measured by the proposed sensor. We could successfully obtain the time when the CBT reached its lowest point, which was at about 5 o'clock, after which it gradually increased toward morning. The mean square error for the tympanic temperature was 0.05 °C, and the correlation coefficient was 0.93. As seen from the Bland–Altman plot in Fig. 15b, the proposed sensor had a small systematic error but a high correlation with the tympanic temperature during sleep.

3.7.3 Jet Lag Monitoring

Next, Fig. 16 shows the CBT changes in a person who returned to Japan after staying in the UK for about a week. The red line represents the normal daily CBT variation for the person in Japan, while the blue line represents the CBT variation immediately after returning from the UK. The time when the CBT reached its minimum shifted from 4:00 to 9:00, a difference of about 5 h, whereas the time difference between

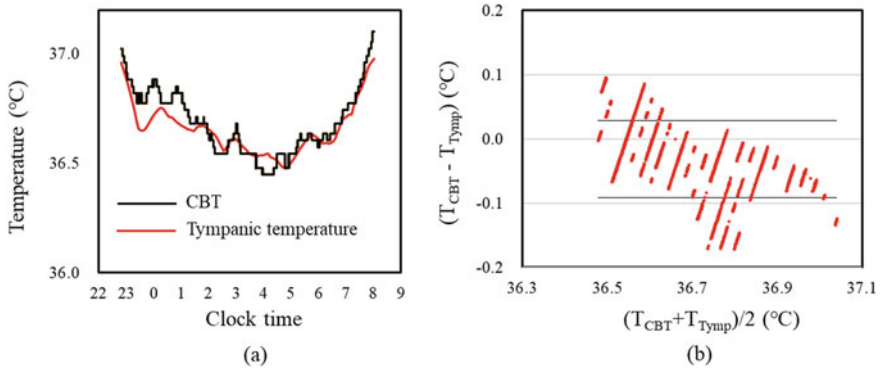

Fig. 15 Sleep demonstration: **a** behavior of the CBT and the reference tympanic temperature, and **b** Bland–Altman plot

the UK and Japan was 7 h. Shifts in circadian rhythms can be visualized from CBT changes, as illustrated in Fig. 17. It has been reported that phase shifts in the circadian rhythm are modulated by external stimuli such as light and food [40]. For example, a phase response curve provides an index for evaluating how much the circadian rhythm shifts depending on the time of light exposure [41]. In particular, Minors et al. reported the shift time for the circadian rhythm with respect to the difference between the time when the CBT reaches its minimum and the time of light exposure. According to this notion, if the body is exposed to light before the time when the CBT is at its lowest, the phase is delayed, whereas if the body is exposed to light after that time, the phase is advanced. Here, the time of the lowest CBT in England was about 9 o'clock, which suggests that the phase was delayed when the person was exposed to the morning sun in Japan. In other words, the jet lag, which should be set back only 5 h, would be expected to shift back 19 h. As this example shows, visualization of the time of the lowest CBT can provide an efficient method for correcting jet lag. This application has a high potential to help improve the quality of life for people who lead irregular lives, such as workers with varying shifts.

3.7.4 Fever Monitoring

Since 2019, vaccination has been a focus in fighting the COVID-19 pandemic, but many people have developed fever after being vaccinated. Thus, we also demonstrated CBT measurement after COVID-19 vaccination. Figure 18a, b show the CBT changes after vaccination and a Bland–Altman plot, respectively. The tympanic temperature was also measured and compared in the same manner as in the previous demonstration. The measurements were started after vaccination, and an antipyretic was taken around 16:00 when the CBT was at its maximum. The results confirmed that the CBT rose for several hours after vaccination and then dropped after the antipyretic was taken.

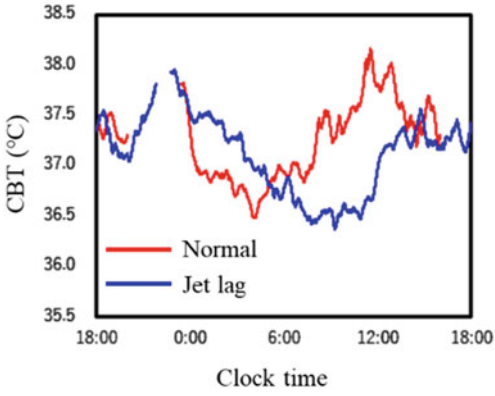

Fig. 16 Comparison of CBT behavior under normal and jet-lag conditions

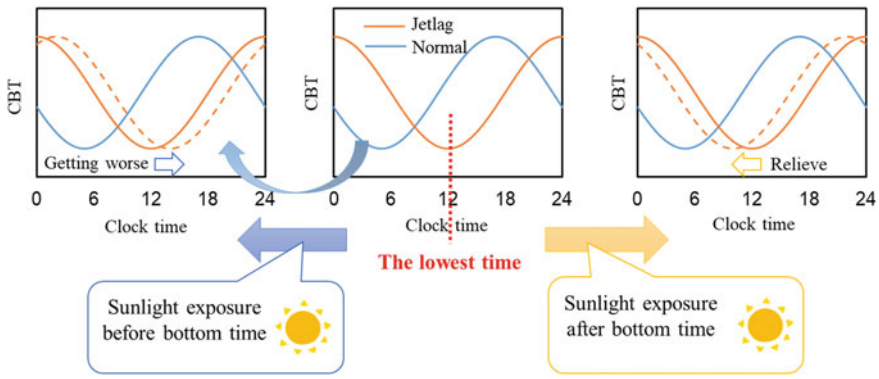

Fig. 17 Illustration of the CBT's circadian phase shift with sunlight exposure

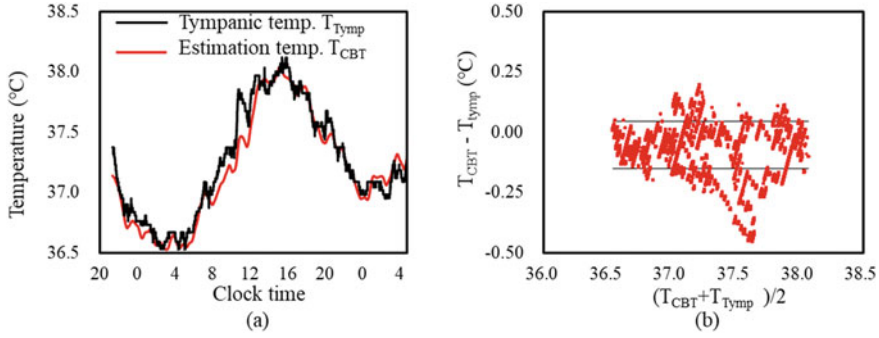

Fig. 18 Fever demonstration: **a** behavior of the CBT and the reference tympanic temperature, and **b** Bland–Altman plot

3.8 Conclusion

We have introduced a technology for estimating the core body temperature (CBT) by using heat flux, with the goal of developing a noninvasive CBT thermometer that can be attached to the body surface. This CBT measurement technique for daily life would be expected to find use in health management systems and new medical applications such as chronopharmacology. Furthermore, if we could visualize the circadian rhythm from CBT fluctuations and understand its deviations from daily rhythms, it would be possible to develop applications that appropriately maintain circadian rhythms through environmental control linked to smart homes.

References

1. Costa, G.: The impact of shift and night work on health. Appl. Ergon. **27**(1), 9–16 (1996)
2. Komarzynski, S., Bolborea, M., Huang, Q., Finkenstädt, B., Lévi, F.: Predictability of individual circadian phase during daily routine for medical applications of circadian clocks. JCI Insight **4**(18) (2019)
3. Scales, W.E., Vander, A.J., Brown, M.B., Kluger, M.J.: Human circadian rhythms in temperature, trace metals, and blood variables. J. Appl. Physiol. **65**(4), 1840–1846 (1988)
4. Tobaldini, E., Fiorelli, E.M., Solbiati, M., Costantino, G., Nobili, L., Montano, N.: Short sleep duration and cardiometabolic risk: from pathophysiology to clinical evidence. Nat. Rev. Cardiol. **16**(4), 213–224 (2019)
5. Hashimoto, S., Nakamura, K., Honma, S., Tokura, H., Honma, K.: Melatonin rhythm is not shifted by lights that suppress nocturnal melatonin in humans under entrainment. Am. J. Physiol.-Regul., Integr. Comp. Physiol. **270**(5), R1073–R1077 (1996)
6. Lévi, F., et al.: Circadian timing in cancer treatments. Annual Rev. Pharmacol. Toxicol. **50**, 377–421 (2010)
7. Higuchi, S., Motohashi, Y., Liu, Y., Ahara, M., Kaneko, Y.: Effects of VDT tasks with a bright display at night on melatonin, core temperature, heart rate, and sleepiness. J. Appl. Physiol. **94**(5), 1773–1776 (2003)
8. Takasu, N.N., Hashimoto, S., Yamanaka, Y., Tanahashi, Y., Yamazaki, A., Honma, S., Honma, K.I.: Repeated exposures to daytime bright light increase nocturnal melatonin rise and maintain circadian phase in young subjects under fixed sleep schedule. Am. J. Physiol.-Regul., Integr. Comp. Physiol. **291**(6), R1799–R1807 (2006)
9. Jean-Louis, G., Kripke, D.F., Cole, R.J., Elliott, J.A.: No melatonin suppression by illumination of popliteal fossae or eyelids. J. Biol. Rhythms **15**(3), 265–269 (2000)
10. Talo, H., Macknin, M.L., VanderBrug Medendorp, S.: Tympanic membrane temperatures compared to rectal and oral temperatures. Clin. Pediatrics **30**(4_suppl), 30–33 (1991)
11. Sund-Levander, M., Forsberg, C., Wahren, L.K.: Normal oral, rectal, tympanic and axillary body temperature in adult men and women: a systematic literature review. Scand. J. Caring Sci. **16**(2), 122–128 (2002)
12. Sund-Levander, M., Grodzinsky, E.: Time for a change to assess and evaluate body temperature in clinical practice. Int. J. Nurs. Pract. **15**(4), 241–249 (2009)
13. Mazerolle, S.M., Ganio, M.S., Casa, D.J., Vingren, J., Klau, J.: Is oral temperature an accurate measurement of deep body temperature? A systematic review. J. Athl. Train. **46**(5), 566–73 (2011)
14. Taylor, N.A., Tipton, M.J., Kenny, G.P.: Considerations for the measurement of core, skin and mean body temperatures. J. Therm. Biol. **46**, 72–101 (2014)

15. Yoshida, S., Miyaguchi, H., Nakamura, T.: Development of tablet-shaped ingestible core-body thermometer powered by gastric acid battery. IEEE Sens. J. **18**(23), 9755–9762 (2018)
16. Kalantar-Zadeh, K., Ha, N., Ou, J.Z., Berean, K.J.: Ingestible sensors. ACS Sens. **2**(4), 468–483 (2017)
17. Byrne, C., Lim, C.L.: The ingestible telemetric body core temperature sensor: a review of validity and exercise applications. Br. J. Sports Med. **41**(3), 126–133 (2007)
18. Nemoto, T., Togawa, T.: Improved probe for a deep body thermometer. Med. Biol. Eng. Comput. **26**, 456–459 (1988)
19. Fox, R.H., Solman, A.J., Isaacs, R., Fry, A.J., MacDonald, I.C.: A new method for monitoring deep body temperature from the skin surface. Clin. Sci. **44**(1), 81–86 (1973)
20. Yamakage, M., Namiki, A.: Deep temperature monitoring using a zero-heat-flow method. J. Anesth. **17**, 108–115 (2003)
21. Mäkinen, M. T., Pesonen, A., Jousela, I., Päivärinta, J., Poikajärvi, S., Albäck, A., ... Pesonen, E.: Novel zero-heat-flux deep body temperature measurement in lower extremity vascular and cardiac surgery. J. Cardiothorac. Vasc. Anesth. **30**(4), 973–978 (2016)
22. Eshraghi, Y., Nasr, V., Parra-Sanchez, I., Van Duren, A., Botham, M., Santoscoy, T., Sessler, D.I.: An evaluation of a zero-heat-flux cutaneous thermometer in cardiac surgical patients. Anesth. Analg. **119**(3), 543–549 (2014)
23. Kitamura, K.I., Zhu, X., Chen, W., Nemoto, T.: Development of a new method for the noninvasive measurement of deep body temperature without a heater. Med. Eng. Phys. **32**(1), 1–6 (2010)
24. Zhang, Y., Chad Webb, R., Luo, H., Xue, Y., Kurniawan, J., Cho, N.H., Rogers, J.A.: Theoretical and experimental studies of epidermal heat flux sensors for measurements of core body temperature. Adv. Healthc. Mater. **5**(1), 119–127 (2016)
25. Huang, M., Tamura, T., Tang, Z., Chen, W., Kanaya, S.: A wearable thermometry for core body temperature measurement and its experimental verification. IEEE J. Biomed. Health Inf. **21**(3), 708–714 (2016)
26. Tamura, T., Huang, M., Yoshimura, T., Umezu, S., Ogata, T.: An Advanced internet of things system for heatstroke prevention with a noninvasive dual-heat-flux thermometer. Sensors **22**(24), 9985 (2022)
27. Pennes, H.H.: Analysis of tissue and arterial blood temperatures in the resting human forearm. J. Appl. Physiol. **1**(2), 93–122 (1948)
28. Yoon, G.H.: Topological design of heat dissipating structure with forced convective heat transfer. J. Mech. Sci. Technol. **24**(6), 1225–1233 (2010)
29. Lazarov, B.S., Schevenels, M., Sigmund, O.: Topology optimization considering material and geometric uncertainties using stochastic collocation methods. Struct. Multidiscip. Optim. **46**, 597–612 (2012)
30. Wang, F., Lazarov, B.S., Sigmund, O.: On projection methods, convergence and robust formulations in topology optimization. Struct. Multidiscip. Optim. **43**, 767–784 (2011)
31. Sigmund, O., Maute, K.: Topology optimization approaches: a comparative review. Struct. Multidiscip. Optim. **48**(6), 1031–1055 (2013)
32. Incropera's Principles of Heat and Mass Transfer. Western John Wiley & Sons Inc., pp. 405–407 (2017)
33. Tanaka, Y., Matsunaga, D., Tajima, T., Seyama, M.: Robust skin attachable sensor for core body temperature monitoring. IEEE Sens. J. **21**(14), 16118–16123 (2021)
34. Moran, J.L., Peter, J.V., Solomon, P.J., Grealy, B., Smith, T., Ashforth, W., Wake, M., Peake, S.L., Peisach, A.R.: Tympanic temperature measurements: are they reliable in the critically ill? A clinical study of measures of agreement. Crit. Care Med. **35**(1), 155–164 (2007)
35. Brajkovic, D., Ducharme, M.B.: Confounding factors in the use of the zero-heat-flow method for non-invasive muscle temperature measurement. Eur. J. Appl. Physiol. **94**, 386–391 (2005)
36. Mariak, Z., Lewko, J., Luczaj, J., Polocki, B., White, M.D.: The relationship between directly measured human cerebral and tympanic temperatures during changes in brain temperatures. Eur. J. Appl. Physiol. **69**, 545–549 (1994)

37. Fulbrook, P.: Core body temperature measurement: a comparison of axilla, tympanic membrane and pulmonary artery blood temperature. Intensive Crit. Care Nurs. **13**(5), 266–272 (1997)
38. Casa, D.J., Becker, S.M., Ganio, M.S., Brown, C.M., Yeargin, S.W., Roti, M.W., ... Maresh, C.M.: Validity of devices that assess body temperature during outdoor exercise in the heat. J. Athl. Train. **42**(3), 333 (2007)
39. Vongsavan, N., Matthews, B.: Some aspects of the use of laser Doppler flow meters for recording tissue blood flow. Exp. Physiol.: Transl. Integrat. **78**(1), 1–14 (1993)
40. Tahara, Y., Shibata, S.: Circadian rhythms of liver physiology and disease: experimental and clinical evidence. Nat. Rev. Gastroenterol. Hepatol. **13**(4), 217–226 (2016)
41. Minors, D.S., Waterhouse, J.M., Wirz-Justice, A.: A human phase-response curve to light. Neurosci. Lett. 133(1), 36–40 (2016) (1991)